

See discussions, stats, and author profiles for this publication at: <https://www.researchgate.net/publication/231531975>

Measuring the Temperature Width of a First-Order Single Crystal to Single Crystal Phase Transition Using Solid-State NMR: Application to the Polymorphism of 2-(2,4-Dinitrobenzyl)-3...

ARTICLE in JOURNAL OF THE AMERICAN CHEMICAL SOCIETY · NOVEMBER 1999

Impact Factor: 12.11 · DOI: 10.1021/ja991204m

CITATIONS

42

READS

25

6 AUTHORS, INCLUDING:



Shifi Kababya

Technion - Israel Institute of Technology

29 PUBLICATIONS 523 CITATIONS

SEE PROFILE



Yoav Eichen

Technion - Israel Institute of Technology

108 PUBLICATIONS 3,479 CITATIONS

SEE PROFILE

Measuring the Temperature Width of a First-Order Single Crystal to Single Crystal Phase Transition Using Solid-State NMR: Application to the Polymorphism of 2-(2,4-Dinitrobenzyl)-3-methylpyridine

A. Schmidt*,[†] S. Kababya,[†] M. Appel,[†] S. Khatib,[†] M. Botoshansky,[†] and Y. Eichen*,^{†,‡}

Contribution from the Department of Chemistry and Solid State Institute, Technion-Israel Institute of Technology, Haifa 32000 Israel

Received April 15, 1999. Revised Manuscript Received September 16, 1999

Abstract: Polymorphism and phase transitions in 2-(2,4-dinitrobenzyl)-3-methylpyridine were investigated using ¹³C and ¹⁵N solid-state NMR, crystallographic, and calorimetric techniques. The coexistence of two phases, **A** and **B**, over at least 8–9 K around the first-order phase transition temperature is observed by solid-state NMR and by following the decay kinetics of a thermally activated tautomerization process in a single crystal. The observations are interpreted in terms of a distribution of mesoscopic domains within the crystal, differing in their local pressure. The presence of dynamic processes on time scales shorter than minutes is excluded by both NMR measurements and tautomerization kinetics.

Introduction

Polymorphism in molecular crystals and the transformation of one phase into another has attracted significant scientific and technological attention over the years.¹ In classical thermodynamics theory, a first-order phase transition takes place when the free energies of the two phases, **A** and **B**, in question, G_A and G_B , become equal. Normally, this condition is fulfilled along a curve representing the intersection between the two free energy surfaces of the two phases. Consequently, at any $T \neq T_c$ (where T_c is the transition temperature at a given pressure), only one phase, **A** or **B**, exists in the sample. The two phases coexist in equilibrium at T_c , exhibiting an infinitely sharp transition at a T_c, P_c pair. As a result, at this temperature, discontinuities appear for all extensive physical properties in the system (entropy, volume, enthalpy, etc.), and the heat capacity of the system becomes infinitely high.

Nevertheless, as early as the 1930s, nonclassical phase transition behavior was observed between polymorphs with structurally similar packing. Work published by Ubbelohde² and others³ around the middle of the century revealed that, at least for molecular crystals, the classical phase transition description is somewhat too simplistic, and many systems can be described only by an expanded set of rules. A considerable number of molecular crystals were shown to exhibit different types of "premonitory effects", "smearing", and hysteresis, where the different crystal phases exhibit gradual onset and offset of physical properties such as heat capacity and volume.² In several cases, these nonclassical phenomena were found to span a

relatively large temperature range.⁴ The deviation from classical behavior was attributed to fine microscopic details that are not accounted for in the classical thermodynamic theory or to factors giving rise to nonequilibrium conditions.

Two basic models aimed at accounting for such nonclassical transitions were proposed, taking into consideration microscopic phenomena.² The initiation of a first-order phase transition around T_c is induced by the nucleation of one phase inside the other. In one model, the transition progresses by domain growth, while in the second model, growth of the new phase is facilitated by the segregation of mobile microscopic domains.

In both models, one must consider the potential energy arising from the need to fit a domain of the new phase into the structurally different lattice of the old phase. This potential energy can be divided into two major contributions: (A) interfacial energy, σ_{ij} , arising from the structural mismatch between the phase lattices in the two-domain interface, and (B) strain energy, ξ_{icj} , generated from the mismatch between the molar volumes of the two lattices. This strain is manifested by either compression or tension, depending on the direction of the transition relative to the volume change. In one direction, the newly formed domains are compressed within the smaller available space of the old phase (thus introducing increased compression), while in the other direction, tension is exerted. Both energy terms depend also on the domain sizes and vary in magnitude as the transition progresses.

The complex and asymmetric nature of these two contributions gives rise to the hysteresis often observed in such cyclic phase transitions. The overall free energy of a given phase is described in eq 1:²

$$G_i = f_i(P, T, \sigma_{ij}, \xi_{icj}) \quad (1)$$

The directional difference in the free energy is represented by

(4) (a) Konno, M.; Sato, Y. *Acta Crystallogr. B* **1975**, *31*, 2007. (b) Boerio-Goates, J.; Westrum, E. F. *J. Mol. Cryst. Liq. Cryst.* **1980**, *60*, 249. (c) Ubbelohde, A. R. *Modern Thermodynamical Principles*; Oxford University Press: Oxford, UK, 1952. (d) Barrie, P. J.; Groombridge, C. J.; Grossel, M. C.; Weston, S. C. *Chem. Commun.* **1992**, 1216.

[†] Department of Chemistry.

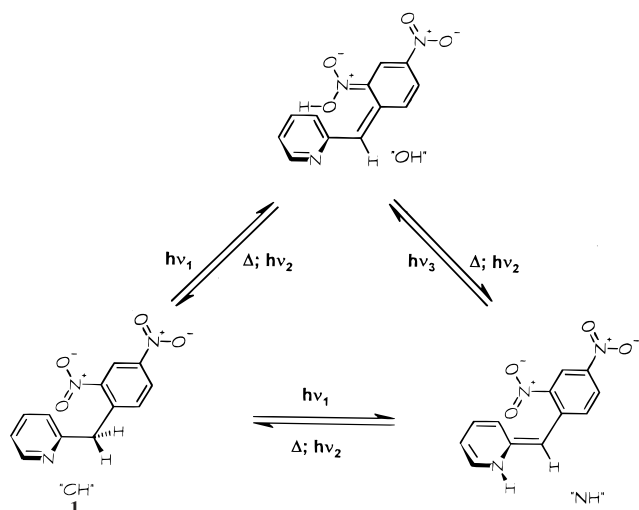
[‡] Solid State Institute.

(1) (a) Herbstein, F. H. Varieties of Polymorphism. Presented at the 18th European Crystallographic Meeting, Prague, Czech Republic, August 1998. (b) Threlfall, T. *Analyst* **1995**, *120*, 2435. (c) *Polymorphism and Polytypism in Crystals*; Verma, A. R., Krishna, P., Eds.; Wiley: New York, 1966. (d) *Pharm. J.* **1998**, *261*, 150. (e) Gavezzotti, A. *Acc. Chem. Res.* **1994**, *27*, 309. (f) Dunitz, J. D.; Berenstein, J. *Acc. Chem. Res.* **1995**, *28*, 193.

(2) (a) Ubbelohde, A. R. *J. Chim. Phys.* **1966**, *62*, 33. (b) Ubbelohde, A. R. *Q. Rev.* **1957**, *11*, 246. (c) Ubbelohde, A. R. *Z. Phys. Chem.* **1963**, *37*, 183.

(3) Frenkel, J. *J. Chem. Phys.* **1939**, *7*, 538.

Scheme 1



the following equations:

$$\Delta G(T)_{i \rightarrow j} = xG_i + (1-x)G_j \quad (2)$$

$$\Delta G(T)_{j \rightarrow i} = (1-x)G_i + xG_j \quad (3)$$

These additional contributions to the free energy surfaces were suggested to give rise to the nonclassical phase transition behavior.² Earlier reports² attributed the deviation from classical first-order phase transition behavior to the formation of “metastable” states in which $\Delta G \neq 0$. These states may be either kinetically “frozen” or may advance to completion of the transition, overcoming “kinetic resistance”. These models and their interpretation were supported by many experimental observations of a variety of nonclassical phenomena in solid-phase transformations.⁴ Despite these early reports and later extensive research in this field, the origin and nature of such nonclassical transformations are not fully understood, mainly due to the limited understanding of the contribution of intermolecular potentials to the thermodynamic functions.

Our interest in such nonclassical phase transitions arises from the need to gain detailed structural information on photoactive crystals, as part of an ongoing effort to correlate the supramolecular structure of assemblies of molecules with their chemical and physical properties. Recently we reported⁵ on the investigation of site selectivity in phototautomerization processes taking place in crystals of 2-(2,4-dinitrobenzyl) pyridine (**1**) derivatives (Scheme 1).⁶ Our preliminary results suggest that the kinetic parameters of such solid-state processes are controlled by neighboring molecules. Even subtle differences in the packing of the molecules in the crystal lattice significantly affect the relative reactivity of the different phototautomers. This effect was attributed to the differences in the ability of neighboring molecules to participate in the tautomerization reaction.⁷ In one system, 2-(2,4-dinitrobenzyl)-3-methylpyridine (**2**), a biexponential decay curve of the phototautomer in the crystal was observed throughout the phase transition temperature range. This observation can be explained if the same “NH” phototautomer is embedded in two phases related by a nonclassical phase transition.

Here we report on a detailed crystallographic, calorimetric and solid-state NMR investigation of the three polymorphs of **2** and the phase transitions between them. The real temperature width of the single crystal to single crystal phase transition taking place between two of the polymorphs is investigated using solid-state NMR techniques.

Experimental Section

Materials. ¹⁵N-Nitric acid (65%, 99% ¹⁵N, Isotec Inc., Matheson USA), 2-amino-3-methylpyridine (Aldrich), deuterated ethanol (CH₃-CH₂OD, 99.5% D, Sigma), and other materials used for the preparation of the different compounds were used as received unless noted. THF was dried over potassium and benzophenone under argon until blue. Triethylamine was distilled over sodium and used immediately.

2-(2,4-Dinitrobenzyl)-3-methylpyridine (2**)** was prepared according to a previously reported procedure.⁵

2-(2,4-Dinitrobenzyl)-3-methylpyridine-*d*₂ (2-d**₂).** Five-hundred milligrams (1.85 mmol) of 2-(2,4-dinitrobenzyl)-3-methylpyridine (**1**) were dissolved in a mixture of 5 mL of dry THF, 10 mL of deuterated ethanol (CH₃CH₂OD, 0.17 mol), and one drop of dry triethylamine. The solution was stirred for 1 week at 50 °C in the dark. Solvents were removed under reduced pressure, and the product was recrystallized from deuterated ethanol (CH₃CH₂OD). The product was deuterated exclusively at the benzylic position (95–98% D by NMR). Mp: 118.8 °C (uncorrected, ethanol). MS (+DCI): 275.9 (M + H⁺). ¹H NMR (200 MHz, CDCl₃): δ 2.34 (s, 3H), 7.1 (t, 1H), 7.45 (s, 1H), 7.48 (d, 1H), 8.2 (d, 1H), 8.4 (d, 1H), 8.87 (d, 1H). ¹³C NMR (50 MHz, CDCl₃): δ 18.8 (s), 39.0 (br s), 120.3 (s), 122.1 (s), 126.9 (s), 131.4 (s), 134.0 (s), 137.9 (s), 141.5 (s), 146.8 (s), 149.5 (s), 155.1 (s).

2-(2,4-Di-¹⁵N-nitrobenzyl)-3-methylpyridine-¹⁵N₂ (2**(¹⁵NO₂)₂).** Six-tenths of a gram of 2-benzyl-3-methylpyridine was added to a mixture of 1 mL of ¹⁵N-nitric acid (65%) and 10 mL of sulfuric acid and then heated to 100 °C with stirring. After 1 h, the solution was cooled to room temperature, quenched with ice, and made basic using an ammonium hydroxide solution. The product was extracted with dichloromethane, dried over sodium sulfate, and chromatographed over alumina (60/40, hexane/ether). The product was isolated as colorless crystals, 0.62 g, 69% yield. Mp: 122 °C (ethanol). MS (+DCI): 276.0 (M + H⁺). ¹H NMR (200 MHz, CDCl₃): δ 2.34 (s, 3H), 4.57 (s, 2H), 7.1 (t, 1H), 7.45 (s, 1H), 7.48 (d, 1H), 8.2 (d, 1H), 8.4 (d, 1H), 8.87 (d, 1H). ¹³C NMR (100 MHz, CDCl₃): δ 18.8 (s), 39.0 (s), 120.3 (s), 122.1 (s), 126.9 (s), 131.4 (s), 134.0 (s), 137.9 (s), 141.5 (s), 146.5 (d), 146.8 (s), 149.5 (d), 155.1 (s). All products were kept in the dark and recrystallized before use.

Apparatus. Calorimetry experiments were performed on a differential scanning calorimeter (DSC, Polymer Science Ltd.). Transient optical absorption spectra were recorded on a Cary 1E instrument (Varian) equipped with a temperature-controlled (Lake Shore 330, Cryotronics), liquid nitrogen-cooled optical cryostat (Oxford, DN1704). X-ray diffraction data were collected at 293 K (**A**, **C**) and at 343 K (**B**) on a Philips PW 1100 four-circle diffractometer. Solution ¹⁵N, ¹H, and ¹³C NMR spectra were recorded on 200 MHz AC200 and 400 MHz wide-bore AM400 spectrometers (Bruker).

Crystal Structures. Crystals of **C** were grown by slow evaporation of 1:1 (v/v) hexane/ether solutions in the dark. Crystals of **A** were grown from ethanol solutions in the dark. Crystals of **B** were obtained by gradually heating a single crystal in phase **A** on a temperature-controlled goniometer head mounted on the X-ray diffractometer. Crystals of phase **C** were grown from hexane/ether solutions. The **A** → **B** single crystal to single crystal phase transition was followed by monitoring the intensities of 25 independent reflections at different temperatures. Significant changes in the intensities of different reflections were observed during a period of up to several days after the phase transition. No solution could be derived from data sets collected at *T*_c and *T*_c + 5 K, even after a period of several days. Satisfactory solution could be

(5) Scherl, M.; Haarer, D.; Fischer, J.; DeCian, A.; Lehn, J.-M.; Eichen, Y. *J. Phys. Chem.* **1996**, *100*, 16175.

(6) Sixl, H.; Warta, R. *Chem. Phys.* **1985**, *94*, 147.

(7) Eichen, Y.; Botoshansky, M.; Peskin, U.; Scherl, M.; Haarer, D.; Khatib, S. *J. Am. Chem. Soc.* **1997**, *119*, 7167. (b) Peskin, U.; Khatib, S.; Eichen, Y. Manuscript in preparation.

Table 1. Crystallographic Information on the Different Polymorphs

	phase A	phase B	phase C
space group	$P2_1/c$	$P2_1/c$	Cc
a (Å)	11.333(4)	11.617(3)	23.756(6)
b (Å)	15.386(4)	15.355(5)	7.175(2)
c (Å)	7.639(3)	7.641(3)	15.078(4)
β (deg)	106.07(3)	105.97(3)	102.39(3)
V (Å ³)	1280.0(8)	1310.4(7)	2510.1(12)
Z	4	4	8
D_x (Mg m ⁻³)	1.418	1.385	1.446
θ range (deg)	1.87–25.10	2.25–22.02	2.77–25.01
absorption coefficient (mm ⁻¹)	0.108	0.105	0.11
temperature (K)	293(2)	363(2)	293(2)
crystal form	plate	plate	needle
crystal size (mm)	0.35 × 0.2 × 0.1	0.33 × 0.25 × 0.1	0.4 × 0.15 × 0.1
absorption correction	none	none	none
no. of measured reflections	2170	1739	5010
no. of independent reflections	2170	1594	2305
no. of observed reflections	1779	1041	1112
criterion for observed reflections	$I > 2\sigma(I)$	$I > 2\sigma(I)$	$I > 2\sigma(I)$
R_{int}	0.0000	0.0336	0.0000
range of h, k, l	$-13 \leq h \leq 13$ $0 \leq k \leq 18$ $0 \leq l \leq 8$	$-12 \leq h \leq 11$ $0 \leq k \leq 16$ $0 \leq l \leq 8$	$-28 \leq h \leq 27$ $0 \leq k \leq 8$ $0 \leq l \leq 17$
intensity decay (%)	2.5	10.4	7.3
R_{obs}	0.0506	0.0745	0.0627
wR_{obs}	0.1292	0.1739	0.1104
S	1.019	1.167	1.087
no. of reflections used in refinement	2111	1594	1899
no. of parameters used	226	226	423
$(\Delta/\sigma)_{max}$	0.011	0.003	0.043
ρ_{max} (e Å ⁻³)	0.274	0.178	0.211
ρ_{min} (e Å ⁻³)	-0.263	-0.211	-0.192

obtained only from data collected after a stabilization period of ca. 7 days at 25 K above T_c .

Crystallographic data were collected using a Philips PW1100 four-circle diffractometer using graphite crystal monochromated Mo K α radiation ($\lambda = 0.7107$ Å) with $\omega/2\theta$ scan (scan width, 1.2°; scan rate, 2° min⁻¹). Unit cell parameters were determined by a least-squares fitting of the setting angles of 25 centered reflections. The intensities of three standard reflections were measured every 120 min during the data collection. All non-hydrogen atoms were found by direct methods and refined anisotropically. Hydrogen atoms were found using a difference Fourier map and refined isotropically. Detailed crystallographic information on the different structures is presented in Table 1. Further details on the crystal structures are available on request from the Director of Cambridge Crystallographic Data Center, 12 Union Road, GB-Cambridge CB2 1EZ, UK, on quoting the full journal citation.

Solid-State NMR. Solid-state NMR measurements were carried out on a 300 MHz CMX-Infinity (Chemagnetics/Varian) triple-resonance spectrometer. Double-resonance measurements were performed using Chemagnetics probes having 7.5 mm spinning modules. CPMAS experiments utilized proton decoupling powers corresponding to 80 kHz. The Hartmann–Hahn match was set at 50 kHz for durations of 10 and 5 ms to allow for optimal transferred carbon and nitrogen polarization. Spinning speeds employed were in the 4–5 kHz range, controlled to within ± 2 Hz.

Variable-temperature experiments were performed in the range of 253–383 K. The sample temperature was allowed to stabilize and equilibrate for a period of up to 20 min before data collection. To limit the temperature gradient across the sample to < 1.5 K, the 7.5 mm rotor was only partially filled.⁸ Absolute temperature determination was obtained by following the solid-to-plastic phase transition of 2,3-dimethyl-1,3-propanediol⁹ (NPG) and of 2-hydroxymethyl-2-methyl-1,3-propanediol⁹ (PG) by ¹³C CPMAS NMR. These phase transitions were found experimentally to span a temperature range of less than 1.5 K. The temperature-dependent chemical shift of ²⁰⁷Pb in PbNO₃ was utilized to calibrate the required temperature range. An absolute

temperature determination for the ²⁰⁷Pb chemical shift scale was obtained using the DSC-measured phase transition temperatures of 317 and 361 K under the same experimental conditions (temperature and spinning speed). These gave rise to a 0.82 ppm/K dependence. Recently, similar dependencies of 0.72,¹⁰ 0.75,¹¹ and 0.78¹² ppm/K were reported, yet our temperature determination, being limited to a relatively small temperature range, is probably more accurate. Using the 0.82 ppm/K dependence, we were able to correct the temperature read on the temperature control device to the actual sample temperature over the desired temperature range. The determination of the temperature gradient across the sample relies on the observed line width of ²⁰⁷Pb in lead nitrate. The temperature calibration procedure will be described in details elsewhere.⁸ Chemical shifts of ¹³C and ¹⁵N were referenced to external standards of TMS and solid ammonium sulfate, respectively. In total, 128 and 16 transients were recorded for ¹³C and ¹⁵N CPMAS experiments, respectively. Repetition delay times of 30–60 s and samples of ca. 160 mg were used.

Triple-resonance REDOR and TEDOR NMR experiments, along with a temperature jump experiment, were employed to obtain complete ¹³C and ¹⁵N spectral assignments of **A** and **B**. This report contains the spectral assignments, while a full experimental account will be provided elsewhere.¹³

Results and Discussion

Polymorphs. Molecular crystals of 2-(2,4-dinitrobenzyl)-pyridine (α -DNBP) and its derivatives display a wealth of crystalline phases, of which some are photoactive while others are photoinert. In this work, three different crystalline polymorphs, **A**, **B**, and **C**, of 2-(2,4-dinitrobenzyl)-3-methylpyridine (**2**) were isolated and structurally characterized by means of X-ray crystallography and solid-state NMR techniques. The phase transitions linking the different polymorphs were char-

(10) Van Gorkom, L. C. M.; Hook, J. M.; Logan, M. B.; Hanna, J. V.; Wasylishen, R. E. *Magn. Reson. Chem.* **1995**, *33*, 791.

(11) Bielecki, A.; Burum, D. P. *J. Magn. Reson. A* **1995**, *116*, 215.

(12) Ferguson, D. B.; Haw, J. F. *Anal. Chem.* **1995**, *67*, 3342.

(13) Kababya, S.; Appel, M.; Khatib, S.; Eichen, J.; Schmidt, A. Manuscript in preparation.

(8) Kababya, S.; Appel, M.; Schmidt, A. Manuscript in Preparation.

(9) Wilmet, F.; Ribet, M.; Bernier, P.; Girault, Y.; Elegant, L. *Solid State Commun.* **1990**, *76*, 621.

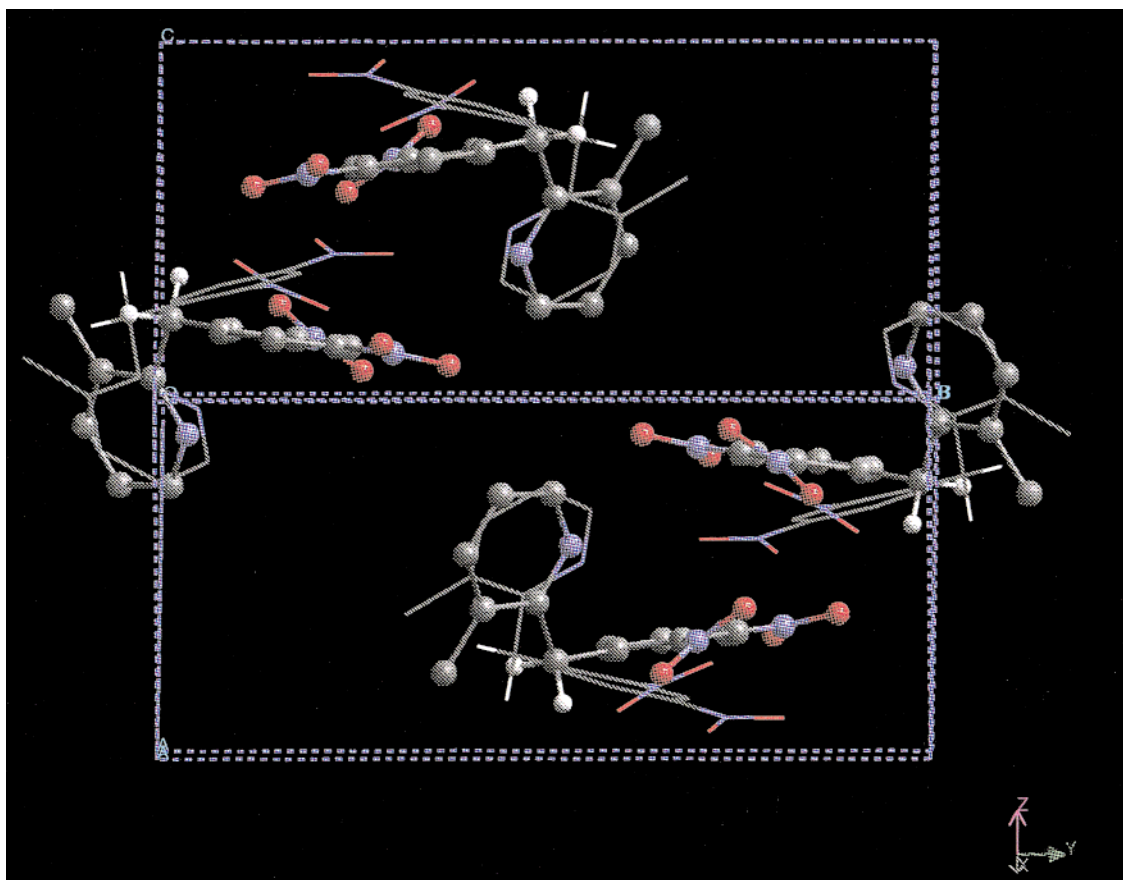


Figure 1. Superposition of the unit cell and molecular packing of **2** in phases **A** (balls and sticks) and **B** (sticks).

Scheme 2

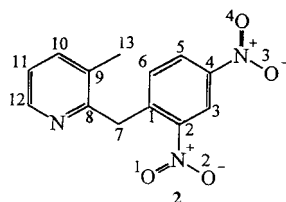


Table 2. Selected Intramolecular Parameters of **2** in the Different Polymorphs

	phase A	phase B	phase Ca	phase Cb
pyridine–phenyl (deg)	56.1(4)	68.3(2)	77.7(4)	83.2(4)
<i>o</i> -nitro–phenyl (deg)	40.8(4)	29.7(8)	14.7(9)	8(1)
<i>p</i> -nitro–phenyl (deg)	14.2(4)	8.2(9)	2.7(6)	21.6(6)
N ₁ –H ₇₁ (Å)	3.12(3)	3.12(7)	3.05(10)	3.02(9)
N ₁ ···H ₇₁ –C ₇ (deg)	42(1)	40(3)	34(5)	41(5)
N ₁ –H ₇₂ (Å)	3.01(3)	2.95(6)	3.07(11)	3.16(10)
N ₁ ···H ₇₂ –C ₇ (deg)	44(1)	49(3)	43(5)	37(4)
O ₁ –H ₇₁ (Å)	2.47(4)	2.38(6)	2.56(10)	2.31(9)
O ₁ ···H ₇₁ –C ₇ (deg)	100(2)	101(4)	94(8)	108(7)
N ₁ –C ₁ –C ₇ –H ₇₁ (deg)	118(2)	130(4)	–156(8)	–155(8)

acterized using calorimetric, X-ray crystallography, and solid-state NMR techniques. The molecular structure and atom numbering of **2** are depicted in Scheme 2.

Phases A and B. A superposition of the packing of the molecules in the unit cells of phases **A** and **B** is presented in Figure 1 (phase **A** in balls and sticks, phase **B** in sticks). Selected intramolecular and intermolecular parameters of the two phases are presented in Tables 2 and 3, respectively. The two phases consist of the same conformer of **2**, differing slightly in its internal coordinates. Crystals of the two phases are colorless, monoclinic, space group *P2₁/c*, with four molecules in the unit cell. The volume of the unit cell of the high-temperature phase,

Table 3. Selected Intermolecular Distances (Å) in the Different Polymorphs of **2**

	phase A	phase B	phase C	symmetry relation
O ₄ ···H [#] ₇₂	3.35(1)	2.80(1)	<i>a</i>	(1 – <i>x</i> , 0.5 + <i>y</i> , 1.5 – <i>z</i>)
O ₃ ···H [#] ₇₂	2.73(1)	2.93(1)	<i>a</i>	(1 – <i>x</i> , 0.5 + <i>y</i> , 1.5 – <i>z</i>)
O ₁ ···H [#] ₇₁	2.88(1)	<i>a</i>	<i>a</i>	(– <i>x</i> , – <i>y</i> , 1 – <i>z</i>)
O _{4a} ···H [#] _{71b}	<i>a</i>	<i>a</i>	3.30(1)	(0.5 + <i>x</i> , 0.5 – <i>y</i> , –0.5 + <i>z</i>)
O _{3a} ···H [#] _{72b}	<i>a</i>	<i>a</i>	2.99(1)	(0.5 + <i>x</i> , –0.5 + <i>y</i> , <i>z</i>)
O _{3b} ···H [#] _{72a}	<i>a</i>	<i>a</i>	2.82(1)	(<i>x</i> , – <i>y</i> , 0.5 + <i>y</i>)
O _{4b} ···H [#] _{72a}	<i>a</i>	<i>a</i>	3.25(1)	(<i>x</i> , 1 – <i>y</i> , 0.5 + <i>z</i>)
O _{2b} ···H [#] _{72b}	<i>a</i>	<i>a</i>	2.54(1)	(<i>x</i> , –1 + <i>y</i> , <i>z</i>)

^a Distance exceeds 3.5 Å or not relevant.

B, is ca. 2% larger than that of phase **A** due to the elongation of the *a* axis. All other unit cell parameters are almost identical in the two phases. The major differences in the molecular structure of **2** in the two polymorphs are manifested by the interplanar angles between the *o*-nitro group, the *p*-nitro group, and the phenyl ring, as well as in the interplanar angle between the pyridine and phenyl rings (see Table 2). In both phases, the oxygen atom of the *o*-nitro group, O₁, is close to one benzylic hydrogen, and the nitrogen atom of the pyridine moiety, N₁, is situated at about the same distance from the two benzylic hydrogens. In phase **B** there is only one close contact between one benzylic proton and a *p*-nitro group of a neighboring molecule. In contrast, in phase **A**, the two benzylic protons interact with oxygen atoms of both *p*- and *o*-nitro groups of neighboring molecules, forming extended –C–H···O– networks.¹⁴ The intermolecular center-to-center distances between the closest ring pairs in each of the phases indicate the absence of any significant π – π interactions between the molecules,

(14) (a) Desiraju, G. R. *Angew. Chem., Int. Ed. Engl.* **1995**, *34*, 2311. (b) Langley, P. J.; Hulliger, J.; Thaimattam, R.; Desiraju, G. R. *New J. Chem.* **1998**, *22*, 1307. (c) Desiraju, G. R. *Acc. Chem. Res.* **1996**, *29*, 441.

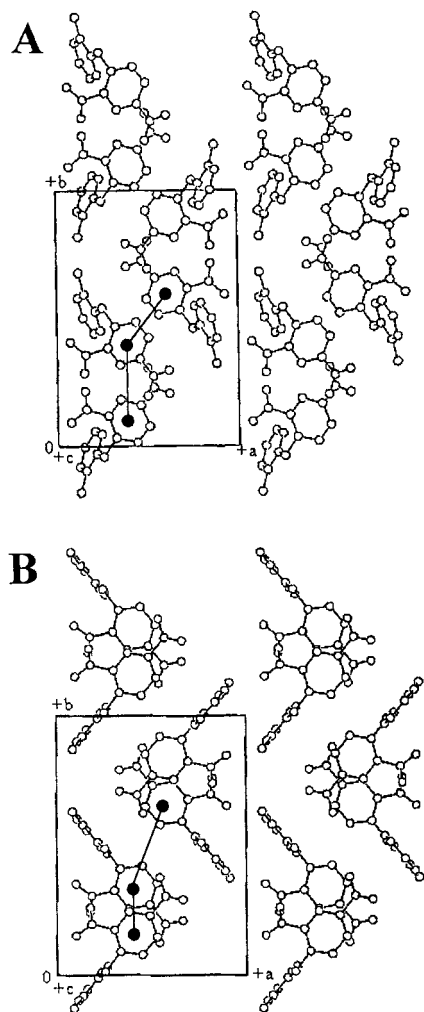


Figure 2. Supramolecular arrangement of **2** in phases **A** (top) and **B** (bottom) viewed along the *c* axis.

$d_{\text{center-center}} > 4.1$ Å. The photoactivity of **2** in the two phases, and the absence of significant π - π interactions with the dinitrophenyl moiety, are in accordance with previous predictions on structure-photoactivity relationship in such systems.¹⁵

Figure 2 depicts the supramolecular arrangement of **2** in phases **A** and **B** along the *c* axis. In both phases, the phenyl groups stack in columns along the *c* axis, separated by 7.64(4) Å (interplanar distance). The phenyl ring centers in one column are shifted by half *c* with respect to the phenyl ring centers of their neighboring molecules in adjacent columns, thus forming interleaved layers. The major difference in the supramolecular packing in the two phases is manifested in the degree of overlap between the interleaved columns. Columns in phase **A** are more evenly spaced than those in phase **B**. Interaxis distances in the two phases are 4.67 and 3.88 Å in phase **A** and 2.71 and 5.34 Å in phase **B**.

Phase C. A stereoscopic view of the molecular packing of **2** in phase **C** is presented in Figure 3. Selected intramolecular and intermolecular parameters are presented in Tables 2 and 3, respectively. Crystals of phase **C** are colorless, monoclinic, space group *Cc*,¹⁶ with two sets of symmetry-related molecules (four of **a** and four of **b**) in the unit cell. The main differences between the nonequivalent molecules are manifested by the interplanar

angles between the *o*- and *p*-nitro groups and the phenyl ring, as well as by the pyridine-phenyl interplanar angle. In the two molecules, one oxygen atom of the *o*-nitro group, O₁, is close to a benzylic hydrogen atom, and the nitrogen atom of the pyridine ring, N₁, is situated at about the same distance from the two benzylic hydrogens. The planes of a pyridine moiety of a **b** molecule and a phenyl moiety of a neighboring **a** molecule are almost parallel, $d_{\text{plane-plane}} = 3.05(1)$ Å. The center-to-center distance between the two rings is $d_{\text{center-center}} = 3.70(5)$ Å. This distance reflects the existence of π - π interactions between the two rings. Crystals of **C** are photoinert, in accordance with previous predictions for systems having π - π interactions between the dinitrophenyl moiety and other ring systems.¹⁵ The molecules are interconnected via -C-H...O- networks formed between benzylic protons and oxygen atoms of neighboring molecules.¹⁴

Calorimetric Investigation. The differential scanning calorimetry (DSC) curves of crystals of **2** and its deuterated analogue **2-d₂** grown from cold ethanol solutions (phase **A**) are presented in Figure 4a and b, respectively. Two sharp endotherms appear in both curves, indicating the presence of two first-order phase transitions. The solid-to-solid **A** \rightarrow **B** phase transitions are found at 318.4 ± 0.2 K for **2** and at 315.0 ± 0.2 K for **2-d₂**. The solid-to-liquid phase transitions (melting points) are found at 396.4 ± 0.2 and $392. \pm 0.2$ K for **2** and **2-d₂**, respectively. Insets in Figure 4a and b depict cyclic DSC measurements of **2** and **2-d₂** in the range of the solid-to-solid **A** \rightleftharpoons **B** phase transition. The cyclic DSC curves exhibit hysteresis, $\Delta T_{\text{peak-peak}} = 9.7 \pm 0.4$ and 9.2 ± 0.4 K for **2** and **2-d₂**, respectively. Clearly, the **A** \rightarrow **B** transition in both **2** and **2-d₂** is characterized by an endotherm with width at half-maximum (WHM) of 3.1 ± 0.4 K, while the reverse **B** \rightarrow **A** transition spans a wider range of temperatures, WHM = 4.8 ± 0.4 K. The solid-to-solid phase transition is reversible. The DSC curves of **2** and **2-d₂** show similar behavior; however, the deuterated analogue undergoes the solid-to-solid **A** \rightarrow **B** phase transition at a lower temperature (ca. -3.5 K). This lowering of the phase transition temperature due to the replacement of the benzylic protons by deuterons suggests that these protons contribute to the packing of the molecules in the crystal and thus to the lattice energy. The predominant intermolecular interactions involving benzylic protons are -C-H...O- networks formed with oxygen atoms of neighboring nitro groups (see Table 3).

Figure 5 depicts the DSC curve of crystals of **2** grown from hexane/ether solutions (phase **C**). Two sharp endotherms are located at 377.8 ± 0.4 and 393.9 ± 0.2 K. These two peaks are separated by an exotherm at 379.2 ± 0.4 K that varies in size with scan rate. The curve indicates the melting of phase **C** at ca. 378 K and its subsequent crystallization as phase **B** at ca. 379 K (phase identity confirmed by solid-state NMR spectroscopy).

In summary, the free energy-temperature diagram revealed by DSC and NMR experiments (*vide infra*) is of a three-crystalline-phase system, as presented in Scheme 3.

NMR Characterization. (i) ¹³C Measurements. The ¹³C CPMAS spectra of polymorphs **A**, **B**, and **C** recorded at 253, 343, and 296 K are presented in Figure 6. The high sensitivity of the ¹³C chemical shifts to the changes in the intra- and intermolecular parameters of the three phases is evident. None of the three solid-state spectra is identical to the proton-decoupled solution spectrum of **2** in CDCl₃ (Table 4). Consequently, the latter provides only limited information for the assignment of the carbon peaks in the spectra of the three solid phases. The complete spectral assignment in such molecular

(15) Khatib, S.; Botoshansky, M.; Eichen, Y. *Acta Crystallogr. B* **1997**, 53, 306.

(16) ¹³C and ¹⁵N NMR investigation support the existence of two nonequivalent molecules in the asymmetric unit.

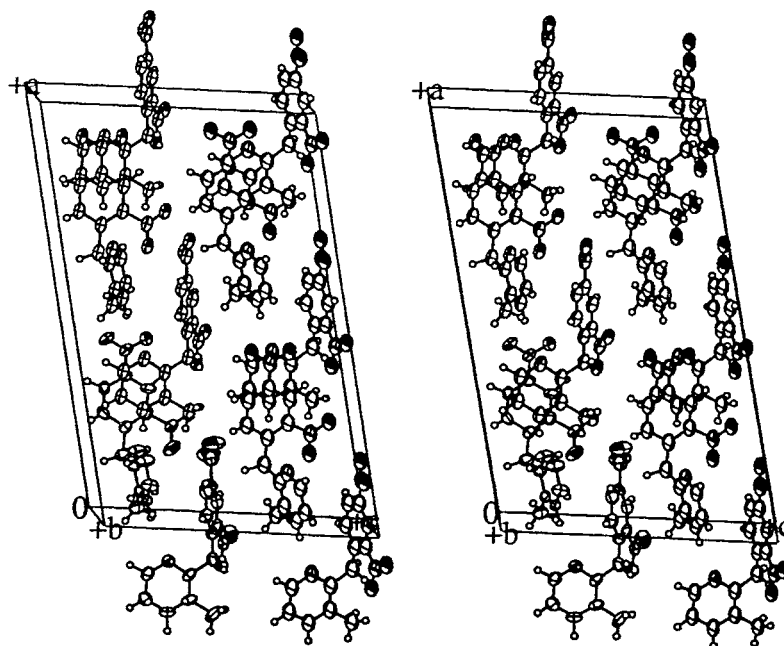


Figure 3. Stereoscopic view of the molecular packing of **2** in phase C.

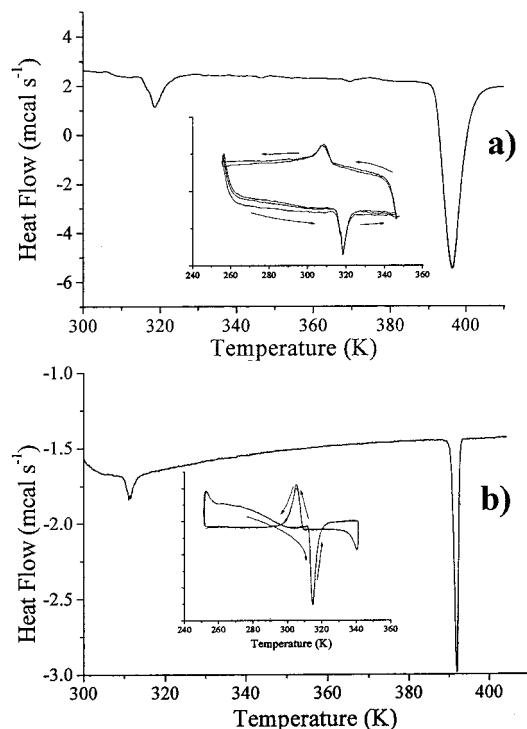


Figure 4. DSC curves of crystals of **2** (a) and **2-d₂** (b) grown from cold dilute ethanol solutions (phase A). Insets: Cyclic DSC measurements in the range of the solid to solid $A \rightleftharpoons B$ phase transition. Sample size, 10 mg; scan rate, 10 K min⁻¹.

crystals is a challenging task. Here it required the tailoring of a variety of NMR techniques, e.g., delayed decoupling, REDOR,¹⁷ TEDOR,¹⁸ and T-jump. A detailed experimental account for the assignments will be given elsewhere.¹³ Complete spectral assignments of phases A and B are presented in Figure 6, and the corresponding isotropic chemical shifts, along with the solution assignment, are summarized in Table 4.

Interestingly, the spectra obtained at temperatures close to T_c are composed of the spectra of both phases A and B. The

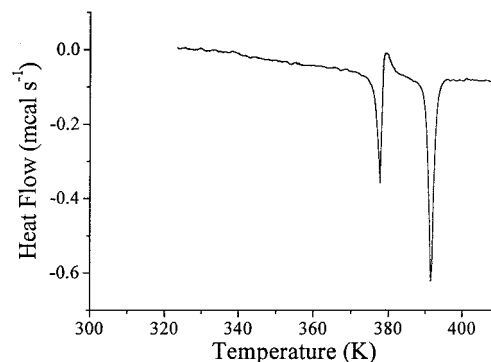
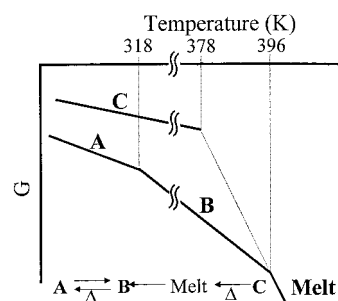


Figure 5. DSC curve of crystals of **2** grown from dilute hexane/ether solutions (phase C). Sample size, 10 mg; scan rate, 20 K min⁻¹.

Scheme 3



ratio between the two spectral contributions is temperature dependent, starting with the spectrum of pure A at $T \ll T_c$ and changing gradually to the spectrum of pure B at $T \gg T_c$. A representative spectrum recorded at an intermediate temperature (313 K) is shown in Figure 6, trace AB. Spectrum AB reflects the coexistence of both phases at 313 K. Detailed examination of the spectra obtained as a function of temperature reveals a gradual and continuous conversion of the low-temperature phase A into the high-temperature phase B. All spectra in the intermediate temperature range were stationary with respect to time course: changing the temperature reestablishes instantaneously (a few seconds for $\Delta T = 1\text{--}2$ K) a new relative composition of the coexisting phases. The resulting spectrum

(17) Gullion T.; Schaefer J. *J. Magn. Reson.* **1989** 81, 196.

(18) Hing, A. W.; Vega, S.; Schaefer, J. *J. Magn. Reson.* **1992**, 96, 205.

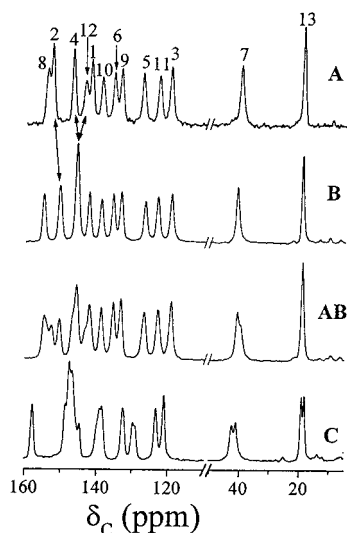


Figure 6. ^{13}C CPMAS NMR spectra of **2** (centerband regions only) recorded at different temperatures: **A**, 253 K; **B**, 343 K; **AB**, 313 K; **C**, 296 K. Experimental parameters: 5 kHz spinning rate; 10 ms contact time, with 50 kHz rf level; 80 kHz decoupling level. About 1000 transients were collected for each spectrum with 30 s repetition time.

Table 4. ^{13}C Chemical Shift Assignments of **A** and **B** Polymorphs and of Solution of **2**^a

carbon no.	phase A	phase B	$\delta_A - \delta_B$	solution (CDCl_3)
1	142	142.4	-0.4	141.5
2	152.8	150.5	2.3	149.5
3	119.6	119.2	0.4	120.3
4	147	145.7	1.3	146.5
5	127.3	126.6	0.7	126.9
6	135.5	135.6	0.1	134.0
7	40.0	41	-1.0	39.0
8	154.1	154.9	-0.8	155.1
9	133.6	133.4	0.2	131.4
10	139	139	0	137.9
11	122.9	123.1	-0.2	122.1
12	143.5	145.7	-2.2	146.8
13	19.2	19.2	0	18.8

^a Chemical shift scale is referenced to TMS.

remains unchanged for periods as long as 24 h. ^{13}C CPMAS shows that, upon cooling the sample, the reverse transition, **B** \rightarrow **A**, is shifted to lower temperatures, in accordance with calorimetric experiments. Both the temperature-dependent spectra and hysteresis are described in further detail in the ^{15}N CPMAS section.

(ii) **^{15}N Measurements.** The assigned ^{15}N CPMAS spectra of phases **A**, **B**, and **C** are shown in Figure 7. All ^{15}N spectra shown in this section correspond to the *o*-nitro and *p*-nitro ^{15}N -labeled samples of **2**. Phases **A** and **B** give rise to ^{15}N spectra with two resolved peaks corresponding to the *o*-nitro (low field) and *p*-nitro (high field) groups. Phase **C**, which consists of two nonequivalent molecules in the asymmetric unit, gives rise to a three-line spectrum with a 1:1:2 intensity ratio. The ^{15}N peak assignment was accomplished for phases **A** and **B** in the solid state and will be described elsewhere.¹³ The corresponding isotropic chemical shift values are listed in Table 5. Phase **C** has not yet been fully assigned. Based on the spectral assignments of **A** and **B**, we attribute the intense high-field peak to the *p*-nitro groups of the two nonequivalent molecules (coincide), and the two lower field peaks to the two nonequivalent *o*-nitro groups.

The high sensitivity of the nitrogen chemical shift to the local environment, and the simplicity of their NMR spectra, render

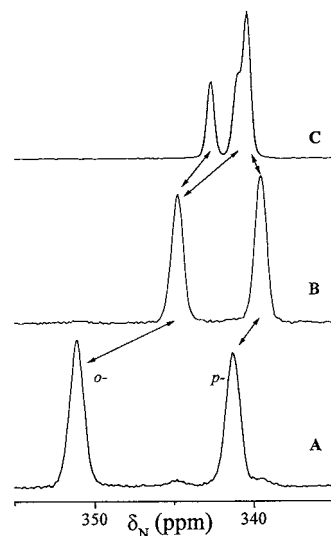


Figure 7. ^{15}N CPMAS NMR spectra of the three polymorphs of **2** (centerband regions only) recorded at different temperatures: **A**, 299 K; **B**, 319 K; **C**, 293 K. Experimental parameters: 3 kHz (**A**, **B**) and 5.4 kHz (**C**) spinning rate; 5 ms (**A**, **B**) and 10 ms (**C**) contact time, with 50 kHz rf level; 80 kHz decoupling level. Up to 40 scans were collected for each spectrum with 30 s (**A**, **B**) and 60 s (**C**) repetition time.

Table 5. ^{15}N Chemical Shift Assignments of **A**, **B**, and **C** Polymorphs and of Solution of **2**^a

	phase A	phase B	$\delta_A - \delta_B$	phase C	solution (CDCl_3)
<i>o</i> -NO ₂	350.9	344.7	6.2	342.7, 341.0	344.7
<i>p</i> -NO ₂	341.1	339.3	1.8	340.5	339.9

^a Chemical shift scale is referenced to solid $(^{15}\text{NH}_4)_2\text{SO}_4$.

it a simple and straightforward probe to scrutinize the phase transition.

To monitor the **A** \rightarrow **B** and **B** \rightarrow **A** phase transformations, ^{15}N CPMAS spectra were recorded as a function of temperature with increments smaller than 1 K over the entire transition temperature range. Starting with a sample of **A** (Figure 7A) and increasing the temperature, the peak intensities of phase **A** gradually decrease while those of **B** gradually increase. A selected set of six spectra, depicting the progression of the **A** \rightarrow **B** transition, is presented in Figure 8. Clearly, the conversion of phase **A** into **B** is continuous, and both phases **A** and **B** coexist over a wide temperature range.

The relative integrated peak intensities of the two phases at each temperature, interpreted in terms of the mole fraction of the phases, are drawn in Figure 9. As can be seen, the phase transition extends over ca. 10 K upon heating (**A** \rightarrow **B**) or cooling (**B** \rightarrow **A**). Upon lowering of the sample temperature, hysteresis is observed, as depicted in the inset of Figure 9. The **B** \rightarrow **A** transition temperature is ca. 7 K lower than the **A** \rightarrow **B** transition temperature.

Accurate temperature calibration and reduction of the sample volume narrows the temperature gradient across the sample to less than 1.5 K. This allows us to set unambiguously a lower limit of 8–9 K for the **A** \rightarrow **B** phase transition span in **2**. The line widths of the resolved ^{15}N peaks of **A** and **B** are 22 Hz over the entire phase transition temperature range. The absence of line broadening across this temperature range excludes the presence of a dynamic process, e.g., two-site exchange of molecules that “hop between phases”, with a correlation time shorter than 1 s. Exchange-NMR SELDOM¹⁹ experiment performed to probe dynamic processes with correlation times on the order of 30 s yielded no evidence for such dynamics.

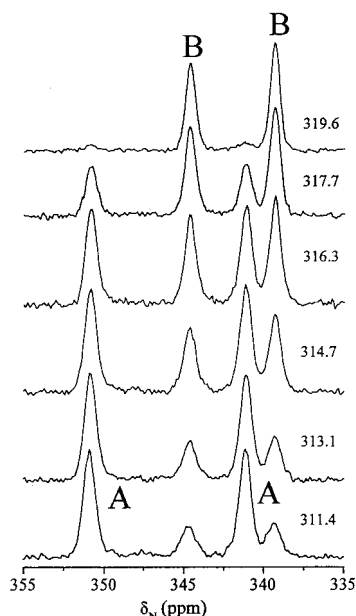


Figure 8. Selected set of CPMAS ^{15}N NMR spectra of **2** as a function of increasing temperature, shown from 311 (bottom) to 319.6 K (top). Experimental parameters: 5 kHz spinning rate; 5 ms contact time, with 50 kHz rf level; 80 kHz decoupling level. Eight scans were collected for each spectrum with 30 s repetition time.

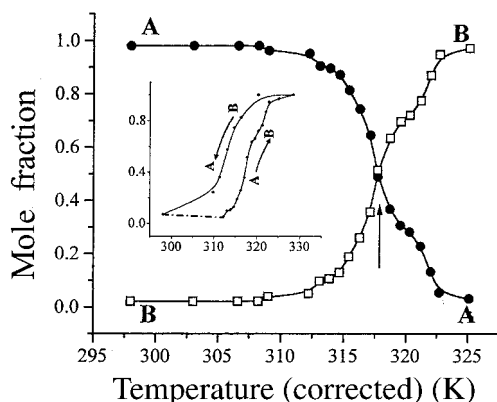


Figure 9. Mole fraction of **A** and **B** phases as a function of increasing temperature, obtained from the integrated peak intensities in the complete set of temperature-dependent ^{15}N CPMAS spectra. Inset: Mole fraction of one component upon heating-cooling cycle.

Therefore, the lower limit for such possible processes is further extended to 1 min. Moreover, no loss of total integrated peak intensity was detected across the phase transition temperature range. This observation excludes the presence of an ill-defined phase, e.g. mobile glass or melt zones, up to the level of our experimental accuracy.

^{15}N CPMAS spectra of phase **C** as a function of its thermal history are depicted in Figure 10. Starting with phase **C** at room temperature (Figure 10a), no spectral changes are detected until 363 K, where the conversion of **C** to **B** commences (Figure 10b). The temperature was set back to room temperature when 90% of phase **C** was converted into phase **B**. Nevertheless, the **C** \rightarrow **B** phase transition proceeded even at room temperature (Figure 10c). Phase **B** is gradually converted into phase **A**, and the process is completed after several months (Figure 10d). The **B** \rightarrow **C** transformation was never observed, in accordance with Scheme 3.

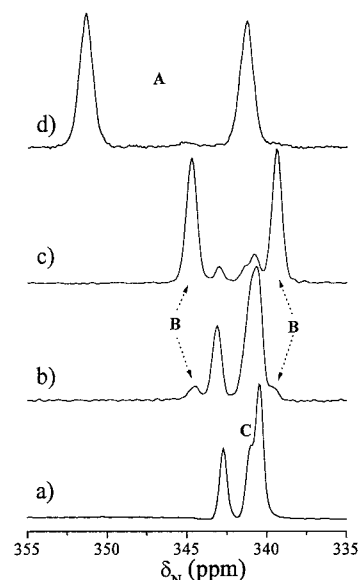


Figure 10. ^{15}N CPMAS NMR spectra of **2** grown from dilute hexane/ether solution (phase **C**) as a function of its thermal history. (a) **C** at 293 K; (b) conversion of phase **C** to **B** commences at 363 K; (c) when 90% of **C** converts to **B**, the temperature is restored to 293 K; (d) after maintaining the sample at 293 K for a period of 3 months. Experimental parameters: 5.4 kHz spinning rate; 10 ms contact time, with 50 kHz rf level; 80 kHz decoupling level. Up to 40 scans were collected for each spectrum with 30 s repetition time.

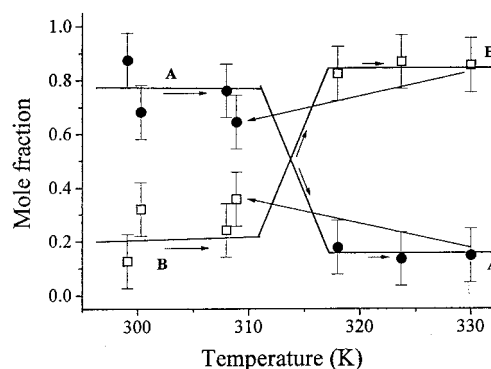


Figure 11. Mole fraction of phases **A** and **B** as a function of temperature in a single crystal of **2**, as obtained from the analysis of the decay of the “**NH**” phototautomers monitored at $\lambda = 611$ nm.

Optical Measurements. Crystals of 2-(2,4-dinitrobenzyl)-3-methylpyridine (**2**) grown from ethanol solutions develop a blue-green color ($\lambda_{\text{max}} = 611$ nm) upon UV irradiation ($\lambda < 430$ nm). This coloration is indicative of a phototautomerization process and the formation of the “**NH**” phototautomer. In all other derivatives of α -DNBP studied so far, the blue-green absorption band decays homogeneously in the dark, displaying a monoexponential behavior. This is indicative of a uniform, thermally activated “**NH**” \rightarrow “**CH**” tautomerization process (Scheme 1). Curiously, in crystals of **2**, the thermal decay of the “**NH**” phototautomer follows a biexponential decay,^{5,7} attributed to the presence of the “**NH**” phototautomers in two coexisting different sites. Investigation of the system revealed that the initial population of the “**NH**” tautomers is strongly temperature dependent (Figure 11).⁷ At temperatures below 310 K, the longer-lived “**NH**” species dominates, whereas at temperatures higher than 320 K, most of the “**NH**” tautomer exists in the short-lived form. Since a very small fraction of the molecules, ca. 10^{-6} , is photoexcited, one can assume that the crystal as a whole is practically unaffected by the pho-

totransformation. Therefore, the two sites reported by the two “NH” populations must originate from differences in the environment offered by the two different phases, **A** and **B**.

If there were to exist interphase exchange processes in the system, decay kinetics measurements imply that their rates are at least one order of magnitude slower than the detected lifetimes (minutes to hours at ambient temperature).

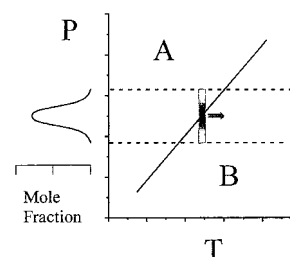
Conclusions

Polymorphism and phase transitions in 2-(2,4-dinitrobenzyl)-3-methylpyridine were investigated using optical, crystallographic, calorimetric, and solid-state NMR techniques. The coexistence of two phases, **A** and **B**, over at least 8–9 K around the first-order phase transition temperature is clearly observed by solid-state NMR and by the “NH” → “CH” tautomerization kinetics in the single crystal. Our X-ray measurements fail to yield any crystallographic structure throughout this phase transition temperature range. While solid-state NMR techniques and kinetic measurements reflect the properties of individual molecular species embedded in their periodical molecular environment, X-ray crystallography requires extended, macroscopic, long-range order to disclose the structure of the molecules in their lattice. Such long-range order does not necessarily exist in our case, where one phase grows from the other.

Solid-state NMR and kinetic data provide evidence for fast response of the system to temperature changes at the molecular level: as a new temperature is set, a new stationary mole ratio of phases **A** and **B** is established instantaneously. Nevertheless, NMR measurements exclude the presence of temperature-dependent fast conformational exchange processes of individual molecules embedded in the crystal lattice. No fast dynamic equilibrium of the type $\mathbf{A} \rightleftharpoons \mathbf{B}$ occurs in the system. This is further supported by the observation of two distinct decay rates in the phototautomer decay kinetics. Hence, the possibility that the phase transition manifests conformational changes of individual molecules embedded in the crystal lattice is excluded. The phase transition, as monitored by the NMR measurements, is therefore described as collective changes of a large number of molecules that constitute domains. Insightful NMR work on phase transitions that dates back to the 1950s utilized ^1H NMR line shapes and second moment analysis to probe and characterize the onset of molecular motion, in particular rotation or tunneling of methyl and methyl-like groups.²⁰ These early studies focused on molecular crystals consisting of small molecules and of species which exhibit a high degree of mobility in the solid state. While onset of motion was often found to correlate with the phase transition phenomena, it does not reflect (as is also indicated by the authors) the cooperative changes that accompany the phase transition.

Solid-state NMR provides yet additional unique and detailed information, revealing the coexistence of the two phases over at least 8–9 K and their gradual interconversion, thus manifesting the nonclassical nature of the phase transition. The slowly evolving intensities of reflections above T_c are attributed to annealing of domains into a long-range ordered system. These observations imply that, in addition to the fast response of the system to temperature changes, much slower processes occur, probably within the multidomain structure. These observations are rationalized in terms of the existence of two different processes having very different time scales. The first process

Scheme 4



constitutes a fast redistribution of the mole ratio of the coexisting phases, while the much slower second process involves macroscopic relaxation of the system. NMR experiments, aimed at a better description and understanding of such slow dynamic processes, are underway.

Microscopically, the overall temperature span of the phase transition can be rationalized by assuming a situation in which different domains undergo the phase transition at a slightly different temperature. This span of transition temperatures may stem from the existence of mesoscopic domains having different surface areas. These domains are characterized by different energy contributions—interfacial, σ_{ij} , and strain, ξ_{icj} —originating from the encapsulation of one phase in the other. NMR measurements clearly show that, at each temperature throughout the phase transition, a new mole ratio of the two phases is reestablished instantaneously (seconds) and is apparently time independent thereafter (24 h). However, X-ray measurements clearly show slow evolution of diffraction patterns (days). Therefore, we suggest that the system rapidly arrives at a local thermodynamic minimum (phase redistribution), after which it slowly evolves to a more stable thermodynamic state (macroscopic annealing).

In this system, local thermodynamic equilibrium is rapidly reinstated at the domain level, and the phase transition temperature span originates from different domains characterized by different T_c values resulting from differences in mesoscopic energy contributions. “Smearing” of the phase transition stems from the distribution of effective P of each domain, where $P_{\text{domain}} = f(P_{\text{ext}}, \sigma_{ij}, \xi_{icj})$. Scheme 4 depicts a schematic P – T phase diagram for **2** in the **A** and **B** space. The distribution in P can be extracted from Figure 9 as the derivative of the mole fraction of **A** as a function of the temperature ($dN(\mathbf{A})/dT$). The overall distribution width is shown by the vertical bar. The gray level in the bar represents the relative abundance of molecules with P_{domain} between P' and $P' + \Delta P$. Increase in temperature is represented by sweeping the bar to the right. At each temperature, the population represented by the portion of the bar above the solid line is in phase **A**, while the portion below the solid line is in phase **B**. Additional aspects of the multiphase system and the effect of crystal packing on proton-transfer tautomerization kinetics are under investigation.

Acknowledgment. This research was supported in part by the Israel Science Foundation, founded by the Israel Academy of Sciences and Humanities, and the Foundation for Promotion of Research at the Technion. Y.E. thanks the US-Israel Binational Science Foundation (BSF) for partial support. S.K. thanks the Lady Davis Fellowship Trust for financial support. The authors wish to express their gratitude to Prof. F. H. Herbstein, Prof. A. Loewenstein, and Dr. U. Peskin from the Department of Chemistry for many fruitful and enlightening discussions.

(20) Gutowsky H. S.; Pake, G. E. *J. Chem. Phys.* **1950**, *18*, 162.